Containerless Solidification and Characterization of Industrial Alloys (NEQUISOL)

2011 J. Phys.: Conf. Ser. 327 012007

(http://iopscience.iop.org/1742-6596/327/1/012007)

Containerless Solidification and Characterization of Industrial Alloys (NEQUISOL)

A Ilbagi[1], H Henein[1,*], J Chen[1], D M Herlach [2,3], R Lengsdorf[3], Ch-A Gandin[4], D Tourret[2,4], A Garcia-Escorial[5]

*Email: hhenein@ualberta.ca

[1]University of Alberta, Edmonton, Canada
[2]Institut für Materialphysik im Weltraum, Deutsches Zentrum für Luft- und Raumfahrt (DLR) Köln, Germany
[3]Institut für Festkörperphysik, Ruhr-Universität Bochum, Germany
[4]Ecole des Mines de Paris, CEMEF UMR CNRS 7635, Sophia Antipolis, France
[5]Dept. Metalurgia Fisica, CENIM-CSIC, Madrid, Spain

Abstract. Containerless solidification using electromagnetic levitator (EML), gas atomization and an instrumented drop tube, known as impulse atomization is investigated for Al-Fe and Al-Ni alloys. The effects of primary phase and eutectic undercooling on the microstructure of Al-Fe alloys are investigated using the impulse drop tube and parabolic flight. The TEM characterization on the eutectic microstructure of impulse-atomized Al-Fe powders with two compositions showed that the metastable Al_mFe formed in these alloys. Also, the growth undercooling that the dendritic front experiences during the solidification of the droplet resulted in variation of dendrite growth direction from <100> to <111>. For Al-4 at%Fe, it was found that in reduced-gravity and in the impulse-atomized droplets the primary intermetallic forms with a flower-like morphology, whereas in the terrestrial EML sample it has a needle like morphology. For Al-Ni, the effect of primary phase undercooling on dendrite growth velocity under terrestrial and reduced-gravity condition is discussed. It is shown that under terrestrial conditions, in the Ni-rich alloys with increasing undercooling the growth velocity increases, whereas in the Al-rich alloys the growth velocity decreases. However, the Al-rich alloy that was studied in reduced-gravity showed similar behavior to that of Ni-rich alloys. Furthermore, the effect of cooling rate on the phase fractions and metastable phase formation of impulse-atomized Al-Ni alloys is compared with EML. A microsegregation model for the solidification of Al-Ni alloys is applied to impulse atomized powders. The model accounts for the occurrence of several phase transformations, including one or several peritectic reactions and one eutectic reaction.

1. Introduction

The properties of materials used in day-to-day activities are governed by their microstructures that form during solidification. Rapid Solidification Processes (RSP) can result in final products with microstructural and constitutional features, which are very different from those obtained under near equilibrium conditions. The unique microstructural features arising from RSP may include formation of microcrystalline structures and decreased grain size or dendrite spacing. The constitutional features may include reduced microsegregation, increased solute solubility and metastable phase formation [1]. All these features have generated strong interest in RSP in recent years.

Understanding the microstructural evolution during solidification is the key to manufacturing products with desired properties. The microstructure evolution during RSP depends on the rate of motion of the solid-liquid interface, which in turn depends on the level of undercooling prior to solidification and the mode of heat extraction. Containerless solidification refers to a class of solidification processes in which large undercoolings are achieved by the complete avoidance of heterogeneous nucleation on container walls. During solidification the heat of crystallization at the solid-liquid interface is released that is conducted into the undercooled melt, i.e. the undercooled liquid acts as a heat sink itself. This gives rise to a negative temperature gradient in front of the solid/liquid interface, which destabilizes a planar solidification front and eventually leads to growth of thermal dendrites. In case of alloys, the concentration gradient enhances the destabilizing effect of the thermal gradient and causes the formation of chemical dendrites.

Presently, computer assisted modeling and simulation of casting processes is used to optimize industrial production routes. In order to develop physically relevant models of solidification, experimental validation is critical. This work focuses on the containerless solidification of industrially important materials such as Al- and Ni- based alloys in terrestrial and reduced gravity conditions [2].

Electromagnetic Levitator (EML), drop tube impulse system, and gas atomization are the containerless processes that have been utilized to investigate the effect of undercooling on eutectic and peritectic reactions. Also, the effect of fluid flow in the dendrite growth dynamics and in the microstructure evolution of solidification will be studied by using EML for comparative investigations in terrestrial and reduced gravity conditions.

EML allows for direct observation of undercooling by contactless pyrometric temperature measurements and measurements of the dendrite growth velocity by using a high speed video camera to observe directly the rapid propagation of the solidification front [3]. It can achieve very high undercoolings in relatively large droplets (~6mm) that solidify in a containerless environment. In this technique the electromagnetic levitation is applied on Earth and in reduced gravity to investigate the fluid flow effects on the dendrite growth dynamics and the microstructure evolution during solidification by post mortem analysis of the as solidified drops. However, EML is limited in the variation of cooling rate that is an important processing parameter to design metallic materials. Complementary experiments of containerless processing of small droplets in drop tube and atomization techniques allow for a change of cooling rate over several orders of magnitude since the cooling rate scales with the droplet size.

Melt disintegration into powder by use of either a mechanical driver (Impulse Atomization (IA)) or high pressure gas (gas atomization) is used to produce powders often of metastable microstructures in masses of several kg. These techniques are very suitable for investigating the formation of various microstructures as a function of droplet size and cooling rate. Using these techniques cooling rates as high as 10^6 K/s is achievable [4].

2. Experiments

2.1. Impulse Atomization

This technique has been developed at the Advanced Materials and Processing Laboratory (AMPL) at the University of Alberta, Canada. Basically, it takes advantage of the fact that a liquid jet emanating from a capillary can be destabilized when disturbed by a particular shock wave with a given frequency. The schematic view of the apparatus is shown in Figure 1. The impulse unit includes a plunger made of refractory material attached to a pulsator which impulses the molten metal through a series of capillaries on the bottom of the crucible. The impulses generate discontinuous streams of molten metal, which in turn break up into droplets. The droplets fall in a static gas atmosphere and solidify as spherical particles [5].

Rapidly solidified particles of two different alloy systems (Al-0.3, 0.93 and 4 at% Fe and Al-20 and 31.5 at%Ni) were produced using this technique. Each alloy of Al-Fe was atomized after achieving 200 K superheat above its respective liquidus temperature. For Al-Ni alloys the superheat was 100 K

above the respective liquidus temperature. The falling particles lost heat during falling to the stagnant helium or nitrogen gas and were collected at the bottom of 4-meter-high drop tube. The collected particles were sieved into different size ranges according to Metal Powder Industries Federation Standard 05 [6].

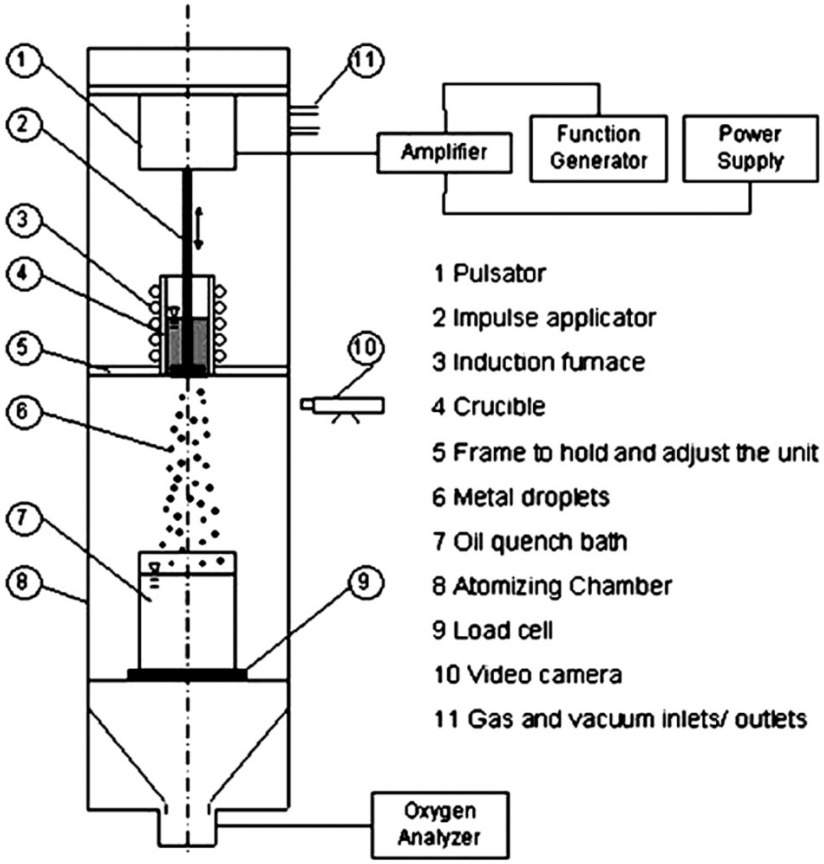

Figure 1. Schematic diagram of the Impulse Atomization tube, also known as drop tube impulse apparatus.

The microstructures of the produced particles were studied using Transmission Electron Microscope (TEM), Scanning Electron Microscope (SEM), Electron Backscatter Diffraction (EBSD), Neutron Diffraction (ND) and X-ray Diffraction (XRD). Rietveld analysis was also used to find the phase fractions in Al-Ni alloys.

The microstructure of impulse-atomized particles of Al-4 at%Fe was compared with the microstructure of an electromagnetically levitated sample solidified in terrestrial and reduced gravity condition. For the experiments under reduced gravity condition, they were conducted by using the TEMPUS facility integrated in an Airbus A300 aircraft for parabolic flight campaign (PFC) at Bordeaux, France.

2.2. Gas atomization

Inert gas atomization is an industrial containerless process where a liquid stream of a molten alloy is disintegrated by high velocity gas. This process yields powder particles in the range 10- 100 μm. The size distribution of the atomized powder particles depends on the processing parameters as gas pressure, metal/gas flow rate, melt superheat, diameter and geometry of the nozzle; on the heat

capacity and thermal conductivity of the gas used; and on the composition, surface tension, density and viscosity of the material to be atomized.

In this work $Al_{68.5}Ni_{31.5}$ were successfully gas atomized in CENIM- CSIC, and the solidification path of the gas atomized powder particles was studied by means of XRD and SEM.

2.3. Electromagnetic levitation

To date EML [1, 2], schematized in Figure 2, is the most suitable technique to levitate stable metallic samples and to achieve direct measurements in deeply undercooled states. An alternating current (AC) flowing through a copper coil produces an electro-magnetic (EM) field. A metallic sample placed within the EM field is levitated by the Lorentz force, FL, which compensates the gravitational force Fg. At the same time, the sample is heated by the Eddy current, Ic. In order to limit the contamination of the melt and the evaporation of light elements the set-up is placed within an ultra-high vacuum chamber, which is evacuated to a pressure of 10^{-8} mbar before backfilling with high purity inert gas (helium 6.0). The droplet is melted and stabilized at several hundred Kelvin above its melting temperature for 10–20 s, which also removes possible residual oxides. Then the current in the coil is rapidly decreased to the minimum necessary for levitation, while cooling gas (He) jets are opened. The current in the coil and the gas jets then remain the same up to complete solidification of the droplet, while the operating pressure is maintained using a vacuum pump.

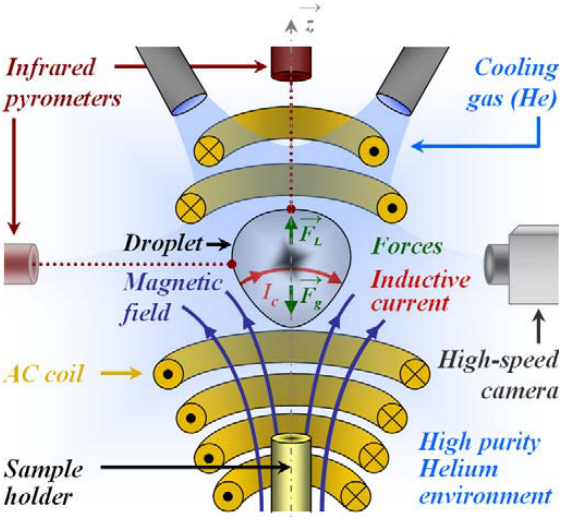

Figure 2. Schematics of the apparatus for electro-magnetic levitation (EML) [7].

During the experiment the temperature of the droplet is measured using a digital infrared pyrometer (Impac IGA10-LO). Solidification involves multiple phase transformations and the identity of the phases encountered by the pyrometer changes. Since the equilibrium temperatures of reactions can be determined from thermodynamic calculations, the emissivity of a sample can be calibrated from its melting curve. Upon heating, the melting of a solid is accompanied by a change in slope of the temperature–time profile due to the heat of melting needed for the transformation from solid to liquid and the change in heat capacities of the existing phases. In addition, levitation experiments enable also measurements of the growth velocity during rapid crystallization of undercooled drops. High-speed camera technique is utilized to measure the velocity V with which the solidification front propagates through the melt. Figure 3 shows a sequence of recorded pictures at various time intervals for an $Al_{50}Ni_{50}$ sample undercooled by 259 K. The high-speed camera is applied both in electromagnetic levitation experiments on Earth and in reduced gravity using the TEMPUS (Tiegelfreies Elektro-Magnetisches Prozessieren Unter Schwerelosigkeit) facility for containerless processing during

parabolic flight campaigns. The dendrite growth velocities of congruently melting $Al_{50}Ni_{50}$ were measured both in 1 g and in reduced gravity.

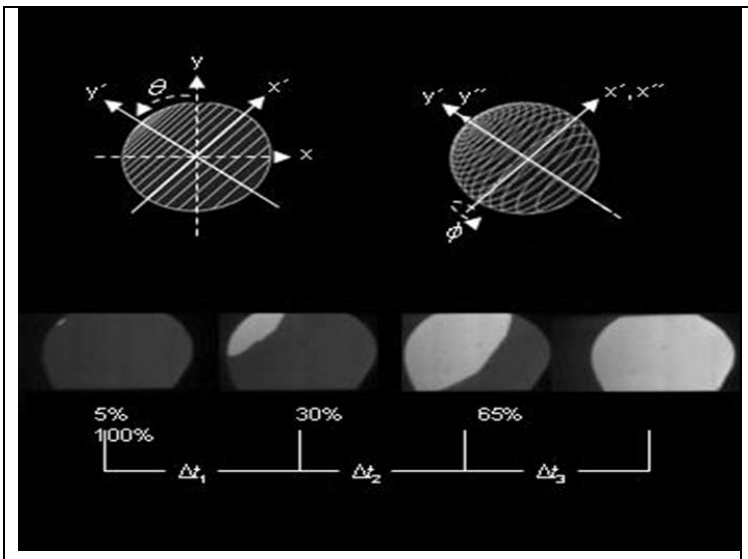

Figure 3. Sequence of high-speed video data taken during the recalescence of a $Ni_{50}Al_{50}$ specimen at an undercooling level of ΔT = 259 K. The present frequency of 30 kHz provides a resolution of 256-128 pixels per frame. The growth velocity can be estimated by dividing each of the real solidification lengths – as obtained from the designated percentages– by the respective solidification time.

3. Metallurgical characterization of samples

3.1. Al-0.3 at%Fe and Al-0.93 at%Fe

The equilibrium solid solubility and diffusivity of iron in the aluminum matrix is very low. The maximum equilibrium solubility of iron in the Al matrix is 0.02 at% at 928 K, the equilibrium eutectic temperature. The eutectic reaction yielding α-Al + Al_3Fe occurs at an iron content of 0.88 at%. The Al_3Fe phase, θ, is later suggested to be $Al_{13}Fe_4$ [8]. This phase is the only equilibrium phase when Fe content is less than 24.4 at% in the binary Al-Fe system and it can be deleterious to the mechanical properties of aluminum alloys.

SEM image from a 355 μm-diameter particle of Al-0.3 at%Fe, produced in nitrogen using the IA technique is shown in Figure 4(a). The nucleation site is highlighted by a circle in this figure. Note the primary trunks radiating from the nucleation site. Figure 4(b) shows the typical eutectic structure at the boundaries of the primary cellular/dendritic α-Al. Figure 4(c) represents the SEM image of an Al-0.93 at%Fe droplet. The microstructure seems similar to Al-0.3 at%Fe, with thicker dendritic/cellular eutectic boundaries because of the higher Fe content in the composition (Figure 4(d)).

Figure 5(a) shows the TEM microstructure of the eutectic area of Al-0.3 at%Fe. Figure 5(b) is a magnified TEM image of a part of the eutectic structure seen in Figure 5(a). Selected Area Electron Diffraction (SAED) and its simulation are shown in Figure 5(d). The diffraction pattern shown in Figure 5(d) is similar to that for Al_mFe (m = 4.0 to 4.4) reported in the literature [10]. Total of 21 SAED simulations were conducted to verify this finding. Comparing the experimentally obtained diffraction patterns and the simulated patterns showed that the intensities of the simulated spots agree well with the intensities (brightness) of the experimentally obtained SAED (see arrows in both obtained [Figure 5(c)] and simulated pattern [Figure 5(d)]). Hence, the Al-Fe intermetallic in the eutectic structure of Al-0.3 at%Fe is Al_mFe. Similar result was achieved for the intermetallic observed in Al-0.93 at%Fe.

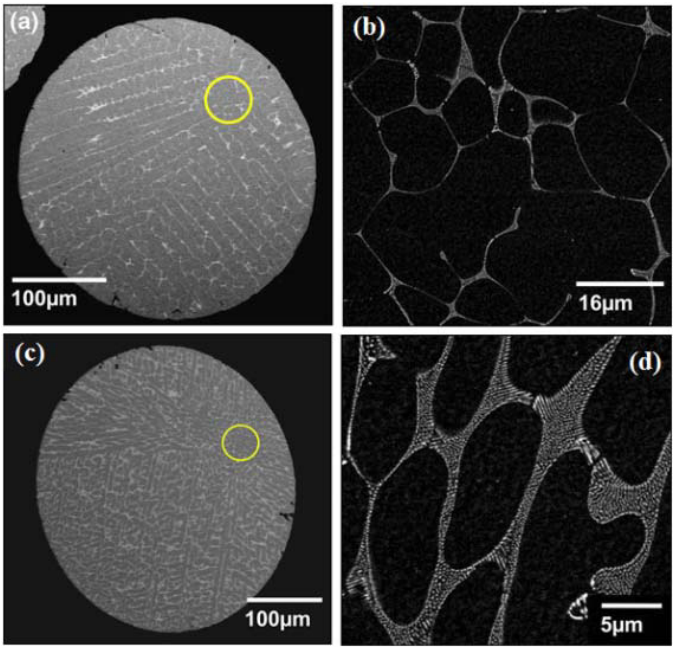

Figure 4. (a) The macrostructure of Al-0.3 at%Fe powder revealed by SEM in backscattering electron mode. Circle shows the area that contains the nucleation site. (b) illustrates the structure of the dendrites/cells at higher magnification, (c) the macrostructure of the Al-0.93 at%Fe droplet similar to that in (a), (d) the magnified image of the eutectic structure seen in (c) [9].

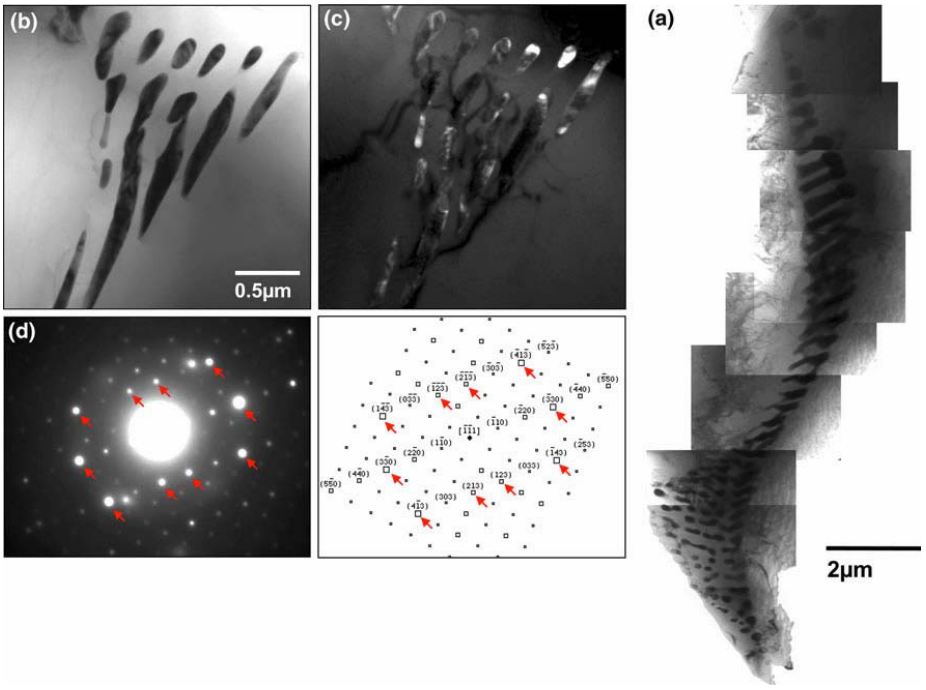

Figure 5. (a) A TEM image of the eutectic structure (b), part of the eutectic structure similar to the one shown in (a). (c) the corresponding dark-field image by choosing reflection (–330). (d) the diffraction pattern and its simulation. The arrows in the simulation correspond to the arrowed spots in the obtained patter shown on the left [9].

One might be surprised by the microstructural similarity between Al-0.3 at%Fe and Al-0.93 at%Fe. According to the equilibrium phase diagram the former is hypoeutectic and the latter is hypereutectic. However, the actual microstructure suggests that the undercooling of the droplet extends the liquidus line of α-Al into the solidus region in the phase diagram, resulting in the solidification of the hypereutectic composition of Al-0.93 at% Fe as a hypoeutectic composition in the metastable phase diagram. Therefore, the phase-formation sequence in Al-0.93 at%Fe is similar to that of Al-0.3 at%Fe (i.e., α-Al is the first solid phase solidified from the melt and eutectic Al_mFe/α-Al is the last structure formed at the end of solidification).

Using image analysis techniques on SEM micrographs the volume fraction of eutectic was measured as a function of Fe content. This measurement was used to estimate the degree of eutectic undercooling. It is found that the undercooling is about 10°C and 17°C for the 0.3 and the 0.93 at% Fe alloys, respectively [11].

Powders with microstructural features similar to those shown in Figures 4 were analyzed using high-resolution EBSD. Three regions were chosen for this analysis. The nucleation site (shown by circle in Figure 4), the trunks emanating from the nucleation site, and the dendrites/cells between the trunks spread over the surface of the droplet were analyzed using EBSD to explore the misorientation between these regions. Results for Al-0.3 at%Fe are shown in Figure 6. Different colors in this image correspond to a different misorientation as a result of different Euler angles. In Figure 6(a), all Euler angles of the nucleation center were chosen as a reference for zero misorientation. It is shown that misorientation for most of the region, especially the three trunks, is within 1 deg. Regions exhibiting colors other than blue correspond to the regions with higher misorientation. Obviously, the regions with a large misorientation are side dendrites/cells with misorientation as high as 10 deg. Also, from the EBSD analysis it was found that a cubic texture exists in both powders with a composition of Al-0.3 at%Fe or with Al-0.93 at%Fe. The dendritic growth direction within the droplets is close to <111>, which is different from the most common <100> in the solidification of cubic alloys. The change in the growth direction has been reported in the literature [12-14] to occur as a result of growth undercooling that the dendritic front experiences during the solidification. This finding confirms the nucleation undercooling discussed by Henein et al. [11].

3.2. Al-4 at%Fe

In this part the microstructure of impulse-atomized particles of Al-4 at%Fe is compared with that of same alloys solidified in EML in terrestrial and reduced gravity condition.

Figure 7 (A) and (B) show the microstructure of Al-4 at%Fe sample solidified under terrestrial and reduced gravity condition (referred as PFC), respectively. The microstructure under different condition is apparently different. The main structure of terrestrial Al-4 at%Fe displays a needle-like morphology of $Al_{13}Fe_4$ while prominent structure of PFC exhibits flower-like $Al_{13}Fe_4$. Figure 7 (C) shows the microstructure of an impulse-atomized droplet of Al-4 at%Fe with the diameter of 925 μm atomized in helium. It is obvious the microstructure is significantly refined compared with those produced using EML both in terrestrial and microgravity condition. Also significant is the morphology of the primary phase, which has the same flower-like morphology with fewer arms. It seems that the liquid stirring due to electromagnetic forces was responsible for the formation of the needle-like primary $Al_{13}Fe_4$. Further investigation on the microstructural evolution and metastable phase formation in this alloy is underway.

3.3 Al-Ni

3.3.1. Impulse Atomization: Comparison between the solidification of $Al_{80}Ni_{20}$and $Al_{68.5}Ni_{31.5}$ alloys is interesting as the former experiences only one peritectic reaction at 854 °C, while the latter goes through two peritectic reactions at 1133 and 854 °C.

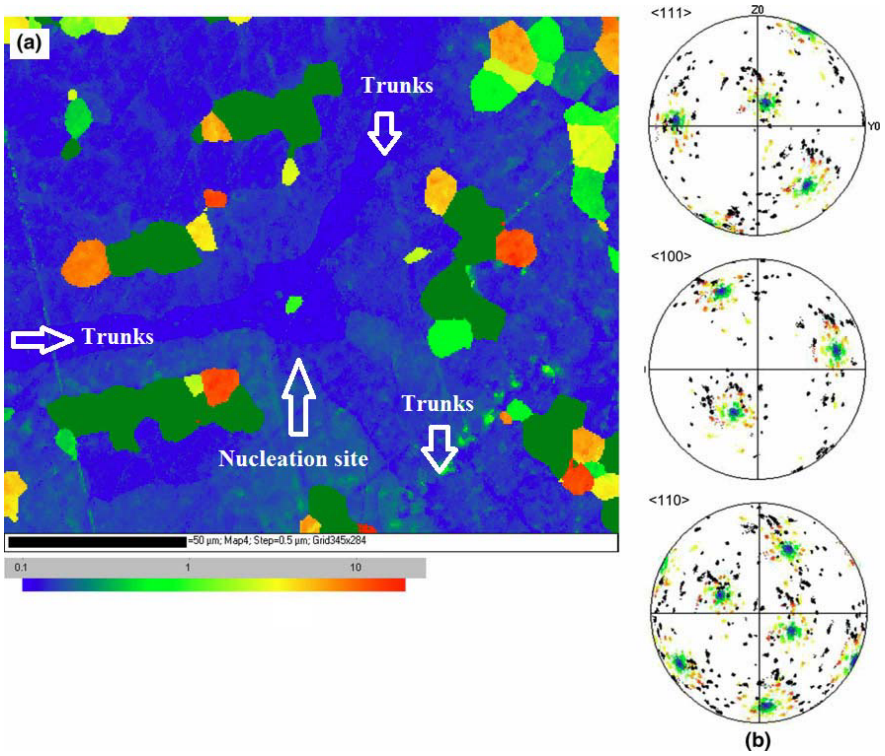

Figure 6. (a) EBSD reconstructed image of the particle shown in Figure 4(a). The orientation (Euler angles) of the nucleation center was chosen as zero misorientation, and then the color in the other area corresponds to the misorientation angle from the nucleation center. The color scheme attached at the bottom of the image shows the misorientation angle (b) illustrates <111>, <100>, and <110> pole figures obtained from the same region. Colors in the pole figures correspond to the region with the same color in (a). In the pole figures, Y_0 and Z_0 are coincident with the primary sample axes [9].

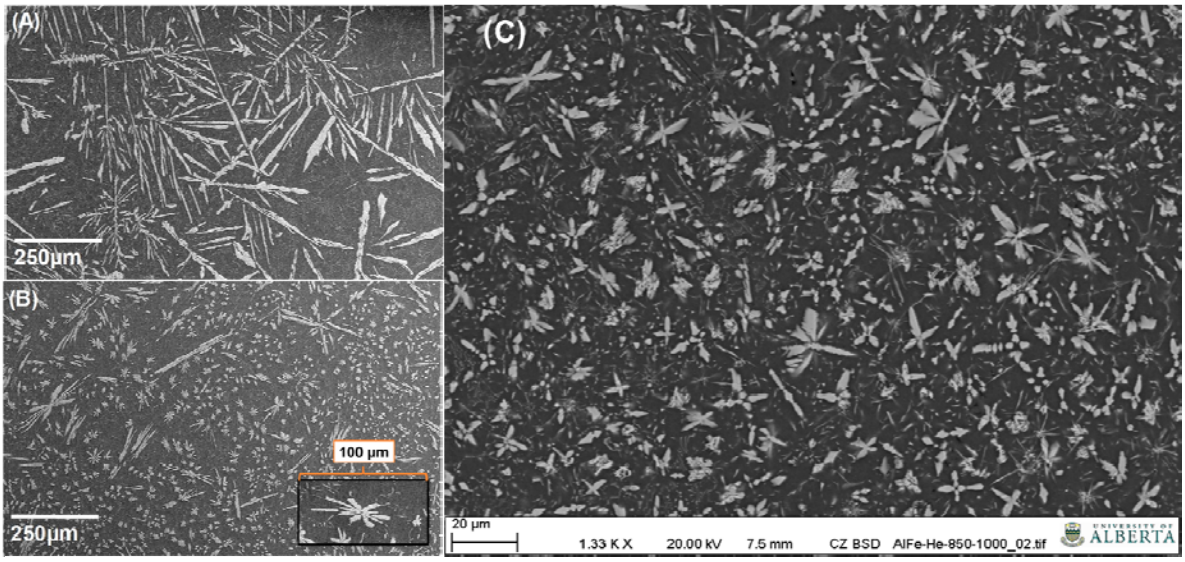

Figure 7. Microstructure of Al-4 at%Fe solidified in (A) EML in terrestrial condition, (B) reduced gravity during parabolic flight, (C) impulse-atomized in helium with diameter of 925 µm.

Powders of $Al_{68.5}Ni_{31.5}$ and $Al_{80}Ni_{20}$ were produced using the impulse atomization technique. Microstructural analysis showed that finer microstructure was achieved in the smaller particle sizes and, also, when helium was used instead of nitrogen.

In particles of $Al_{80}Ni_{20}$ with diameter of 165 μm the formation of primary Al_3Ni_2 was suppressed and Al_3Ni formed directly from the melt. The microstructure of two different sizes of this alloy is shown in Figure 8. It is clear that in Figure 8 (b) no sign of peritectic microstructure can be observed.

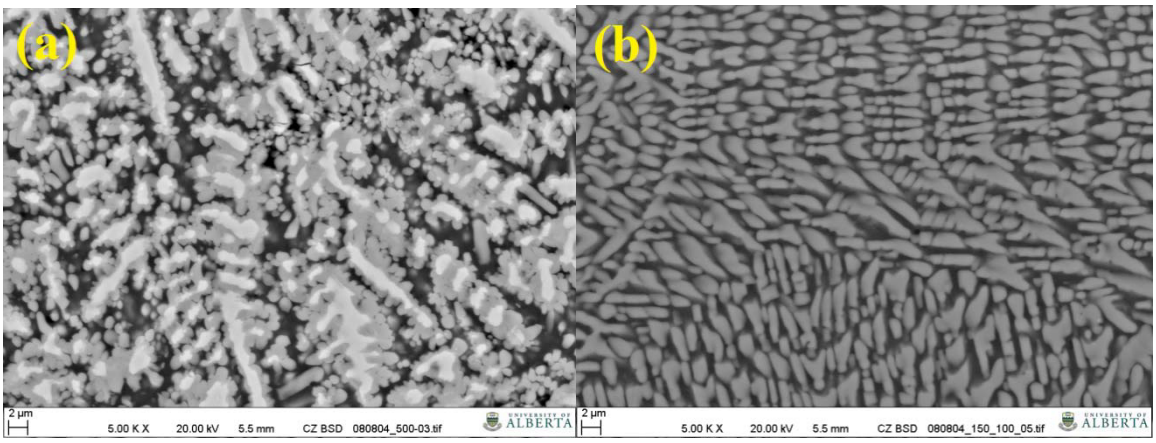

Figure 8. $Al_{80}Ni_{20}$ impulse-atomized in helium (a) D=550 μm (b) D=165 μm

Neutron diffraction investigation of small particles of $Al_{80}Ni_{20}$ also showed that particles with diameter smaller than 275 μm contain some unidentified peaks (e.g. at ~3.5Å^{-1}). Figure 9 shows the neutron diffractogram of three different particle sizes of this alloy. Clearly, the smaller the particle size the more pronounce the unidentified peak. These peaks may correspond to the formation of a quasicrystalline phase known as D-phase [15]. Shuleshova et al. [16], using electromagnetic levitation, showed that this metastable phase forms at undercoolings of 150-200 ºC below the peritectic temperature 854 ºC.

Secondary dendrite arm spacing was used to estimate the solidification cooling rate. The XRD and ND were successfully used to estimate the phase fractions of the solidified powders. For each alloy, the ratio of Al_3Ni to Al_3Ni_2 was calculated from the Rietveld refinement to investigate the effect of cooling rate on the phase fractions after solidification (see Figure 10). In addition, Scheil–Gulliver equation was applied to investigate the extent to which it can predict the phase fractions in these alloys. In $Al_{68.5}Ni_{31.5}$, it was found that by increasing cooling rate, the ratio of Al_3Ni to Al_3Ni_2 approaches that of Scheil–Gulliver's prediction. This was attributed to the suppression of the peritectic transformation at high cooling rates. Opposite behavior was observed in $Al_{80}Ni_{20}$, where the ratio decreased and approached Scheil–Gulliver's prediction with decreasing cooling rate. This observation was related to the direct formation of Al_3Ni from the liquid and the suppression of Al_3Ni_2 formation [17-18]. These trends have been verified with more detailed analysis by ND over a range of particle sizes.

Effect of cooling rate on the lattice parameter of Al_3Ni_2 was also investigated. It is known that the Al_3Ni_2 structure is similar to that of AlNi structure with 33% of the nickel sites vacant at the stoichiometric composition. The vacancies are ordered in a way that every third sheet of nickel atoms perpendicular to one of the threefold axes of the cube is absent. The ordering transforms the crystal structure from cubic to rhombohedral by unequal changes of the parameters *c* and *a*. The cube diagonal in AlNi becomes the *c* axis in Al_3Ni_2 ($c = a'\sqrt{3}$, where a' is the cube edge) and the cube face diagonal becomes *a* axis of Al_3Ni_2 unit cell ($a = a'\sqrt{2}$). Therefore, it is expected that the axial

ratio to be *c/a*=1.225. However, due to the collapse along the *c* axis, as a result of the missing planes, it drops to 1.2132 at stoichiometric Al_3Ni_2. The *c/a* ratio falls continuously across the phase with increasing aluminium content of Al_3Ni_2 [19].

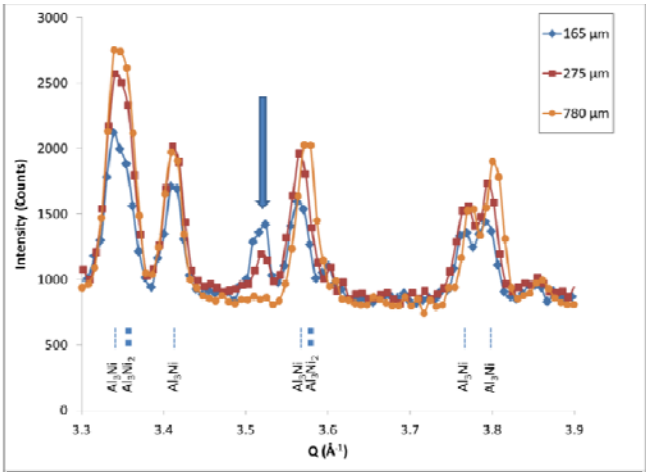

Figure 9. Part of neutron diffractogram of three different particle sizes of impulse-atomized $Al_{80}Ni_{20}$, showing peak position of different phases. Note the unindexed peak at ~3.5Å^{-1}.

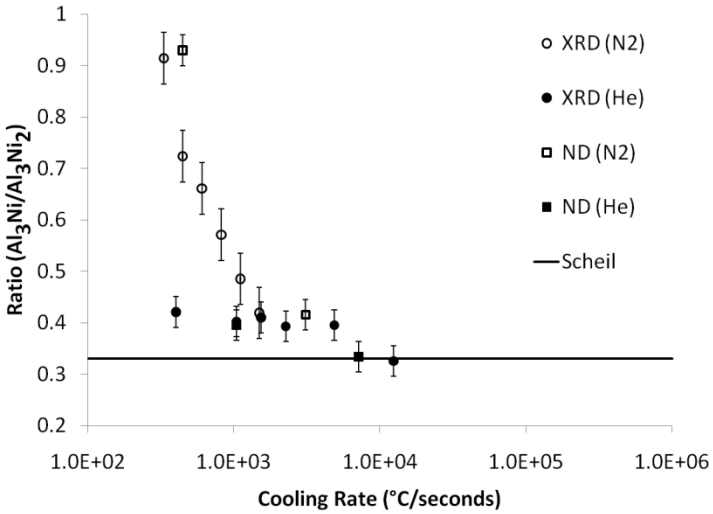

Figure 10. ND and XRD results for the ratio of Al_3Ni to Al_3Ni_2 as a function of cooling rate for two sets of Al-31.5 at%Ni samples. One cooled in helium and the other cooled in nitrogen [18]

Rietveld method was applied to the ND patterns of Al-Ni alloys to find the lattice parameters of Al_3Ni_2 and to investigate the effect of cooling rate on the *c/a* ratio in this phase. The results showed that in $Al_{80}Ni_{20}$, the *c/a* ratio is significantly smaller than the stoichiometric *c/a* ratio of Al_3Ni_2, and it decreased with increasing cooling rate. On the other hand, for $Al_{68.5}Ni_{31.5}$, the *c/a* ratio is much closer to the stoichiometric *c/a* ratio and it increases with increasing the cooling rate.

According to Al-Ni phase diagram and the shape of the Al_3Ni_2 region it is clear that the fraction of nickel within the Al_3Ni_2 that forms from AlNi is higher than that in the Al_3Ni_2 which forms directly from the liquid. This results in an increase of the *c/a* ratio as there are more nickel atoms in the lattice of Al_3Ni_2. Also, it is possible that the observed differences are due to different formation mechanisms

of Al_3Ni_2 in these alloys. In $Al_{80}Ni_{20}$, the Al_3Ni_2 phase nucleates and grows directly from the liquid while in $Al_{68.5}Ni_{31.5}$ it nucleates from the peritectic reaction of AlNi with the liquid and grows both from the peritectic transformation and from the liquid.

3.3.2. EML: The equiatomic intermetallic compound $Al_{50}Ni_{50}$ was subject of recent investigations with respect to the experimental proof of the influence of forced convection on the kinetics of dendrite growth in the regime of low undercooling by comparative investigations on Earth and in reduced gravity [20]. In the present work, we report on measurements of dendrite growth velocities as a function of undercooling on a series of Al–Ni samples of various compositions. The Ni-rich alloys show the usual behavior such that the growth velocity increases with increasing undercooling. In contrast, the Al-rich alloys exhibit a very unusual growth behavior: their growth velocity decreases with increasing undercooling. Such anomalous solidification kinetics has not been reported so far in literature. High undercoolings $\Delta T = T_L - T$, where T_L is the liquidus temperature of the respective alloy, were measured ranging up to $\Delta T \leq 325$ K. Electromagnetic levitation for containerless undercooling in combination with a high-speed video camera was applied to measure the rapid dendrite growth velocity as a function of undercooling for Al–Ni alloys in terrestrial experiments. The TEMPUS facility for containerless processing in reduced gravity [21] was used during the sounding rocket mission TEXUS 44 to measure the dendrite growth velocity of Raney-type $Al_{68.5}Ni_{31.5}$ alloy. One hundred and eighty seconds of reduced-gravity time was available for this particular experiment. Three undercooling and solidification cycles were obtained. The sample was heated by more than 200 K above the liquidus temperature of this alloy, T_L = 1768 K. The sample undercooled during the subsequent solidification cycles to ΔT_1 = 185 K and ΔT_2 = 228 K, respectively. In this way two data points were obtained of dendrite growth velocity measured in reduced gravity. The TEMPUS facility is equipped with a video camera that can capture 200 pictures per second. During recalescence, three pictures were taken, which allow the determination of the growth velocity with an accuracy of ±(15–25)%.

The circles in Figure 11 show results of measurements of dendrite growth velocity as a function of undercooling performed under terrestrial conditions for the series of Al–Ni alloys. In all samples the growth velocity is measured in the undercooling range of 100 K < ΔT < 350 K. The $Al_{55}Ni_{45}$ alloy shows the usual behavior. The dendrite growth velocity increases with increasing undercooling. This behavior is understood by the fact that the driving force for crystallization scales with the undercooling obtained prior to solidification. If 5 at.% Al is added to $Al_{55}Ni_{45}$, the growth velocity of $Al_{60}Ni_{40}$ obviously passes through a minimum at an undercooling of $\Delta T \approx 175$ K. With further increasing the Al content in $Al_{65}Ni_{35}$ alloy, the minimum is shifted to larger undercoolings. In Raney-type alloy $Al_{68.5}Ni_{31.5}$ and for $Al_{70}Ni_{30}$ a monotonous decrease in the growth velocity with increasing undercooling is measured. The alloy with the largest amount of Al, $Al_{75}Ni_{25}$, shows a maximum at $\Delta T \approx 160$ K followed by a continuous decrease of $V(\Delta T)$ up to the largest undercooling ΔT = 315 K. In situ observation of phase selection in undercooled melts of $Al_{68.5}Ni_{31.5}$ alloy by energy dispersive X-ray measurements at the European Synchrotron Radiation Facility Grenoble (France) on levitation-processed drops unambiguously demonstrates that over the entire undercooling range ΔT < 320 K the intermetallic AlNi phase of B2 structure is primarily formed [16]. It subsequently transforms by a peritectic reaction $L + AlNi \rightarrow Al_3Ni_2$. For $Al_{75}Ni_{25}$ alloy, Al_3Ni_2 primarily solidifies from the melt as evidenced by the X-ray diffraction experiments. In situ diffraction investigations indicate that this phase is primarily formed even at highest levels of undercooling. Despite the change in the primary phase formation from AlNi to Al_3Ni_2 at concentrations between 68.5 and 75 at.% Ni, all alloys in this compositional regime show a decrease in growth velocity with increasing undercooling. So far, there is no model that describes such an anomalous growth dynamics-undercooling relation.

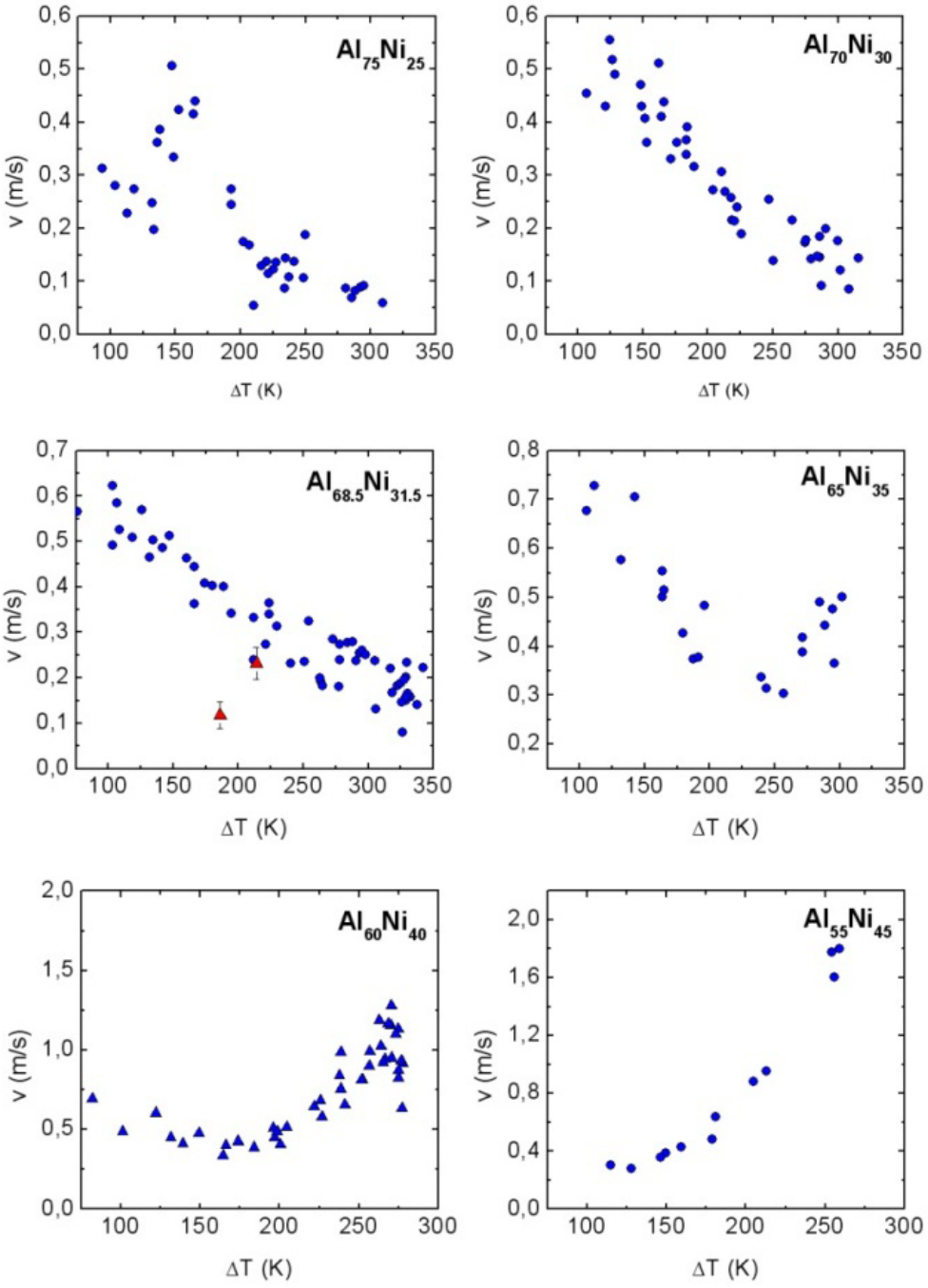

Figure 11. Dendrite growth velocity as a function of undercooling measured under terrestrial conditions (circles) by using high speed video technique on electromagnetically levitated samples of $Al_{100-x}Ni_x$ alloys of concentrations x = 45, 40, 35, 31.5, 30, 25. An anomalous dendrite growth behavior is found for Al-rich Al-Ni alloys such that the growth velocity is decreasing with increasing undercooling. The filled triangles show results obtained under reduced gravity for Raney type $Al_{68.5}Ni_{31.5}$ alloy during TEXUS 44 flight mission.

In previous investigations of the dendrite growth velocity vs. undercooling relation of equiatomic $Al_{50}Ni_{50}$, a pronounced effect of forced convection was found [20]. The growth velocity is observed to be systematically higher in terrestrial experiments than in experiments in reduced gravity. This behavior can be described by an extended sharp interface theory of dendrite growth by introducing Péclet numbers for heat and mass transport due to forced convection in the electromagnetically levitated melt. More details of the extended sharp interface theory are given elsewhere [22]. In the undercooling range in which the growth velocity is smaller than or comparable with the estimated fluid flow velocities in electromagnetically levitated liquid drops, a significant difference was observed in the two complementary sets of experiments. According to estimations by Hyers et al. the fluid flow velocity in liquid drops electromagnetically levitated on Earth is estimated by hydrodynamic calculations to be of the order of 0.5 m s^{-1} [23]. If one compares this value for fluid flow velocity with the range of dendrite growth velocities measured for the differently concentrated Al–Ni samples, it is found that the $Al_{55}Ni_{45}$ sample shows growth velocities that are comparable with or higher than the fluid flow velocity. In case of $Al_{60}Ni_{40}$ alloy the minimum in the V(ΔT) relation occurs at a velocity that is comparable with the fluid flow velocity. In all other Al-rich Al–Ni alloys the measured growth velocities are smaller than the expected fluid flow velocity over the entire range of undercooling accessible by electromagnetic levitation. In order to investigate the influence of forced convection on the dendrite growth behavior we have varied the power of the alternating electromagnetic field within the maximum range that allows levitation of the samples in terrestrial levitation experiments (variation by about 50%). Within the uncertainty of the measurements no influence of the levitation field on the growth velocities vs. undercooling relation was detected. Significantly smaller fluid flow velocities are accessible by processing under reduced-gravity conditions. The Raney-type alloy was studied with respect to dendrite growth dynamics during the sounding rocket mission TEXUS 44 of the European Space Agency (ESA) and the German Aerospace Center (DLR). TEXUS sounding rocket missions provide an excellent quality of reduced gravity of the order of 10^{-4}g. The filled triangles in Figure 11 show the growth velocity V as a function of undercooling of Raney-type $Al_{68.5}Ni_{31.5}$ alloy as retrieved from the TEXUS experiment. Two significant and important differences of the experiments under normal gravity and in microgravity are observed. First, the growth velocity measured in microgravity is substantially smaller than the data taken under 1g conditions. Second, the temperature dependence of the V(ΔT) relation differs. In reduced gravity, it is apparent that the growth velocity increases with increasing undercooling as usual for a great variety of alloys. The decrease in the velocity with undercooling as measured on the ground for a variety of Al-rich Al– Ni alloys is anomalous and unique. By taking into account the results of the TEXUS 44 flight, this anomalous behavior of dendrite growth dynamics of Al-rich Al–Ni alloys is obviously associated with a gravity dependent mechanism in crystal growth in undercooled melts. However, a detailed understanding of the experimental results obtained on Earth and in reduced gravity is still lacking.

3.3.3. Gas Atomization: Direct observations of gas atomized $Al_{68.5}Ni_{31.5}$ powders by SEM showed that they were nearly spherical in shape. Figure 12 shows the surface of the particles of three different sizes, less than 25 μm, 25-50 μm and 50-100 μm. The surface of the particles with diameters below 25 μm was smooth, whereas larger particles presented rougher surfaces, associated with the occurrence of a non-planar solidification front and subsequent solidification.

The X- ray diffraction patterns of the $Al_{68.5}Ni_{31.5}$ powder particles showed that the signal of the Al_3Ni_2 phase decreased when the powder particle size increased, meanwhile the signal of the Al_3Ni phase increased when the powder particle size increased. These results are in agreement with those achieved from impulse atomization of $Al_{68.5}Ni_{31.5}$ shown in Figure 10.

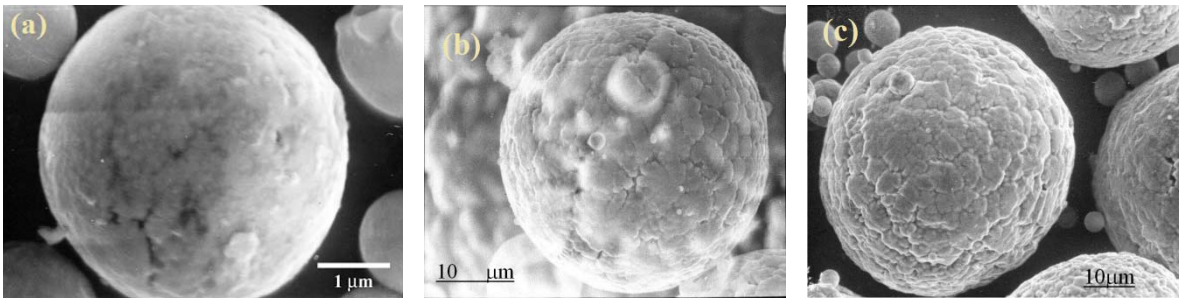

Figure 12. Particles of gas-atomized $Al_{68.5}Ni_{31.5}$ alloy with the following particle sizes: a) <25 µm, b) 25-50 µm and c) 50-100 µm.

4. Modeling

For a given alloy, thermodynamic equilibrium predicts a unique fraction of phases at room temperature, whatever the size of the system. This is obviously not the case in the experimental results presented for atomization. Not only the distribution of phases varies with the diameter of the particles, but it is also found to be a function of the atomization gas. Explanations involve competition between diffusion in phases and growth of dendritic, peritectic and eutectic microstructures, combined at various heat extraction rates. A model developed for the prediction of microsegregation taking place in a uniform temperature system [24] was later coupled with thermodynamic equilibrium calculations and applied to electromagnetic levitation [7] and gas atomization [25]. It is used for the understanding of the several physical effects involved that permit explanations of the measured fractions of phases.

Because the model is presented into details in references [7] and [24], it is only summarized hereafter. The geometry of the system is assumed spherical in shape, with radius corresponding to the particle size. A uniform temperature is considered, as well as constant densities for all phases, resulting in a diffusive regime for heat and mass flows. Nucleation of the dendritic, peritectic and eutectic microstructures takes place at the equilibrium liquidus temperature computed with the liquid composition located at the center of the system. Growth proceeds by radial propagation towards the system periphery. The growth kinetics is computed using available models in the literature [26, 27]. The average total mass and solute mass balances are written in each phase as well as at each phase interface. A global heat balance is yet used thanks to the uniform temperature approximation. Heat extraction takes place through the outer surface of the system. The heat transfer coefficient is calculated with a modified Whitaker correlation developed for impulse atomization [28]. Enthalpies of all phases and interface compositions are computed with the software ThermoCalc using the CALPHAD method [29, 30] and the public binary database PBIN (www.thermocalc.se).

Figure 13 presents the result of simulations performed for atomization of an $Al_{80}Ni_{20}$ alloy corresponding to the particle sizes given in Figure 13. The data used for the simulations are given in Table 1. Each column of Figure 13 stands for one simulation, namely (left) D = 550 µm and (right) 165 µm. The three graphs on each column share the same x-axis and show the time evolution of: (a) the temperature of the droplet, with the equilibrium temperatures for the formation of a new solid phase (horizontal lines with filled symbols) and the predicted nucleation temperatures (horizontal lines with empty symbols); (b) the average volume fraction of the phases and (c) the radius of each zone, i.e. dendritic Al_3Ni_2, peritectic Al_3Ni and eutectic (Al+ Al_3Ni), normalized by the total radius of the particle, R. The normalized radius of a zone illustrates the extent of the expansion of a microstructure within the droplet. For instance, when the radius $R^{Al_3Ni_2}/R$ reaches 1, the mushy zone – or grain envelope of the primary dendritic structure – is fully developed and no bulk liquid remains.

We notice first the difference in cooling rate and the resulting solidification time being inversely proportional to the particle size. Secondly, the predicted nucleation temperature for the peritectic phase is systematically higher than the equilibrium temperature defined by the phase diagram, while

the nucleation of the eutectic occurs close to its equilibrium temperature. We detail hereafter the solidification scenarios for the two simulations, in order of complexity.

4.1. Regime of distinct successive growth

The most common solidification behavior is presented for the larger particle in Figure 13. This solidification scenario is close to those described in earlier publications [7, 24]. The cooling curve exhibits three recalescences, corresponding to the successive growths of the primary dendritic Al_3Ni_2, the peritectic Al_3Ni and the eutectic (Al+ Al_3Ni) microstructures. Direct solidification of the primary dendritic Al_3Ni_2 occurs between t = 20 and 50 milliseconds. The graph (c) with the radii of zones shows that the peritectic zone starts to grow at around t = 40 ms, but its expansion is quickly stopped by the increase in temperature due to the recalescence associated with the primary dendritic Al_3Ni_2 phase shown in graph (a). After the primary recalescence, the temperature decreases again and, at around t = 80 ms, the peritectic zone grows significantly and leads to a peritectic recalescence and a clear increase of the average volume fraction of the Al_3Ni phase as shown in (b). The decrease in primary Al_3Ni_2 fraction is first due to the remelting of the primary solid induced by the peritectic recalescence and then to the peritectic transformation $Al_3Ni_2 \rightarrow Al_3Ni$, which lasts up to complete solidification. After 100 ms, the eutectic structure grows and fills in the remaining liquid. Finally, the solidification is complete when the solid eutectic zone is fully developed, i.e. when R^{Al}/R reaches one.

4.2. Regime of shortcut of the primary growth

On the other hand, the small particle follows a different solidification path as illustrated in Figure 13. The composition gradients involved are of the same order of magnitude, and then the diffusion and growth kinetics are comparable, while the cooling rate is almost one order of magnitude higher. Hence, the growth-induced primary undercooling is so high that the temperature is already below the peritectic nucleation temperature before any primary solid has significantly started to grow. On the radii graph (c), the peritectic zone starts expanding very shortly after the primary mushy zone, but with a higher growth velocity. Hence, the peritectic zone quickly overtakes the primary zone ($R^{Al_3Ni} \geq R^{Al_3Ni_2}$), the growth of the latter then being stopped as the primary dendrites are completely surrounded by the peritectic phase. Additionally, the peritectic recalescence takes place up to temperatures higher than the peritectic equilibrium temperature $T_P^{Al_3Ni}$. After the peritectic recalescence, cooling continues and the solidification ends with eutectic growth. The final microstructure only contains peritectic Al_3Ni and eutectic (Al+ Al_3Ni) as shown in (b).

As can be concluded from a first comparison between the simulated solidification sequence presented in Figure 13 and discussed above, the model predicts well the qualitative phase fractions observed in Figure 8.

5. Summary and conclusion

Containerless solidification behavior of Al-Ni and Al-Fe alloys was investigated under terrestrial and reduced-gravity conditions. Impulse and gas atomization was utilized to investigate the effect of cooling rate on phase fractions and morphology of the evolved phases. In addition, electromagnetic levitation was used to measure the dendrite growth velocity as a function of undercooling for a series of Al-Fe and Al–Ni samples of various compositions. The following results were achieved:

1. The TEM characterization on the eutectic microstructure of impulse-atomized Al-Fe powders with two compositions showed that the metastable AlmFe formed in these alloys. The presence of metastable AlmFe indicates that eutectic nucleation undercooling occurs in the solidification. Also, the fact that the hypereutectic Al-0.93 at%Fe solidifies as a hypoeutectic composition indicates that the nucleation of the α-Al is energetically favored over nucleation of any aluminum iron intermetallics, which is due to primary phase undercooling. Also, the growth undercooling that the dendritic front experiences in the solidification of the droplet resulted in variation of dendrite growth direction from <100> to <111>.

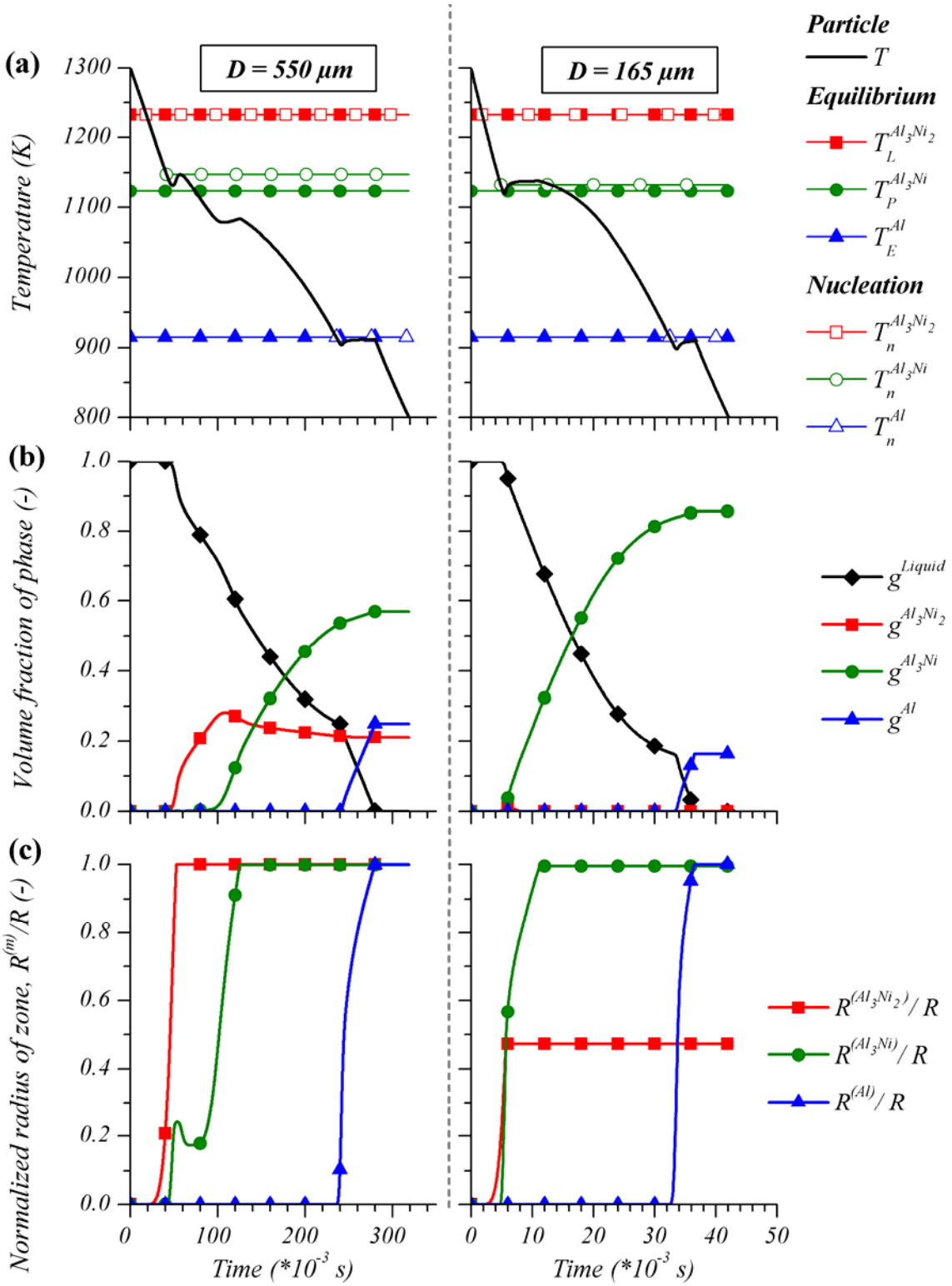

Figure 13. Simulation of the solidification of $Al_{80}Ni_{20}$ impulse-atomized in helium with particle diameter (left) D=550 µm and (right) D=165 µm, with (a) the temperature; (b) the average volume fraction of phases and (c) the normalized radii of the zones, i.e. the position of the growing dendritic, peritectic and eutectic envelopes of the microstructures.

Table 1. Simulation data for Figure 13.

Parameter	Symbol	Value	Unit	Source
ThermoCalc database	-	PBIN	-	
Nominal compositions	x_0	80	at.% Al	
	w_0	64	wt% Al	
Particle diameters	D	(Figure 13a) 550	μm	
		(Figure 13b) 165		
Solid structure diffusion coefficient	D^s	5×10^{-11}	$m^2\ s^{-1}$	[7]
Liquid phase diffusion coefficient	D^l	10^{-9}	$m^2\ s^{-1}$	[7]
Secondary dendrite arm spacing	λ_2	(Figure 13a) 10	μm	
		(Figure 13b) 1		
Solid structure nucleation undercooling	ΔT_n^s	0	K	
Gibbs-Thomson coefficient of solid/liquid interfaces	$\Gamma^{Al_3Ni_2/l}$	$2\ 10^{-8}$	m K	[7]
	$\Gamma^{Al_3Ni/l}$	3.5×10^{-8}	m K	[31]
	$\Gamma^{AlNi/l}$	1.86×10^{-7}	m K	[31]
Eutectic structure contact angle	$\theta^{Al_3Ni/l}$	19.22	°	[31]
	$\theta^{Al/l}$	11.29	°	[31]
External temperature	T_{ext}	293	K	
Droplet initial velocity	v_0	0	$m\ s^{-1}$	
Atomization gas	-	Helium	-	
Density of the particle	ρ	$(w_0/\rho_{Al} + (1-w_0)/\rho_{Ni})^{-1}$	$kg\ m^{-3}$	
Density of Aluminum	ρ_{Al}	2700	$kg\ m^{-3}$	[32]
Density of Nickel	ρ_{Ni}	8909	$kg\ m^{-3}$	[32]
Density of Helium	ρ_f	$37.303\ T^{-0.9559}$	$kg\ m^{-3}$	[28]
Viscosity of Helium	μ_f	$(4.3679\ T^{0.6702})10^{-7}$	Pa s	[28]
Thermal conductivity of Helium	k_f	$0.002778\ T^{0.7025}$	$W\ m^{-2}\ K^{-1}$	[28]
Prandtl number	Pr	0.713	-	[28]
Coefficients in Whitaker's relation	B	2.778×10^{-3}	-	[28]
	m	0.7025	-	[28]

2. For Al-4 at%Fe, it was found that in reduced-gravity and in the impulse-atomized droplets the primary intermetallic forms with a flower-like morphology whereas in the terrestrial EML sample it has a needle like morphology. This was attributed to differences in liquid convection.

3. Quasicrystalline D-phase was observed in impulse-atomized particles of Al80Ni20 with diameter smaller than 275 μm. Also it was observed that with increasing cooling the ratio of Al3Ni to

Al3Ni2 decreases. Opposite behavior was observed In Al68.5Ni31.5. The effect of cooling rate on the lattice parameter of Al3Ni2 was also studied. In Al80Ni20, the c/a ratio is significantly smaller than the stoichiometric c/a ratio and it decreases with increasing cooling rate. On the other hand, for Al68.5Ni31.5, the c/a ratio is much closer to the stoichiometric value and it increases with increasing the cooling rate.

4. Electromagnetic levitation for containerless undercooling was used to measure the dendrite growth velocity as a function of undercooling for Al–Ni alloys in terrestrial condition. The Ni-rich alloys showed the usual behavior such that the growth velocity increases with increasing undercooling while the Al-rich alloys exhibit a very unusual growth behavior. The growth velocity decreased with increasing undercooling. This phenomenon was attributed to a gravity dependent mechanism in crystal growth in undercooled melts as in reduced gravity, the growth velocity increased with increasing undercooling as usual for a great variety of alloys.

5. A microsegregation model for the solidification of binary alloys was used that accounts for diffusion in all phases, as well as nucleation undercooling and growth kinetics of the solidifying microstructures. It successively considers the occurrence of several phase transformations, including one or several peritectic reactions and one eutectic reaction. This model represents a practical tool to study the solidification of alloys that experience multiple phase transformations. It is detailed enough to take into account several phenomena occurring during the solidification (undercooling, growth kinetics, different diffusion length scales, etc.) while leading to quite efficient calculations. It is thus believed to provide a practical solution for application to metallic alloys.

6. The trends observed in phase fractions for Al-Ni alloys in gas atomized powders showed a similar trend to those observed with impulse powders.

6. Acknowledgment

The current work is part of the NEQUISOL project supported by ESA within contract number 15236/02/NL/SH and CSA within contract number 9F007-08-0154 and SSEP Grant 2008.

7. References

[1] Jones H 1983 *Rapid Solidification of Metals and Alloys* (The Institute of Metallurgists, London) p 35
[2] Herlach D M 1991 *Annu. Rev. Mater. Sci.* **21** 23
[3] Herlach D M, Galenko P and Holland-Moritz D 2007 *Metastable Solids from Undercooled Melts* (Pergamon Materials Series)
[4] Zheng B, Lin Y, Zhou Y and Lavernia E J 2009 *Metall. Mater. Trans. B* 40(5) 768
[5] Olsen K, Sterzik G, Henein H 1995 *Third Int. Symp. on Recycling of Metals and Engineered Materials* (The Minerals, Metals, Materials Society, Warrendale, PA) 67
[6] Standard test methods for metal powders and powder metallurgy products 1993 Metal Powder Industries Federation (Princeton, NJ)
[7] Tourret D, Gandin Ch-A, Volkmann T and Herlach D M 2011 *Acta Mater.* **59** 4665
[8] Zhou Y, Juarez-Islas J A, Alvarez-Fregoso O, Yoon W Y, Lavernia E J 1999 *J. Mater. Res.* **14** 729
[9] Chen J, Dahlborg U, Bao C M, Calvo-Dahlborg M and Henein H 2011 *Metall. Mater. Trans. B* Article in Press, 1
[10] Berg B S, Hansen V, Midgley P A and Gjonnes J 1998 *Ultramicroscopy* **74** 147
[11] Henein H, Buchoud V, Schmidt R-R, Watt C, Malakhov D, Gandin C-A, Lesoult G and Uhlenwinkel V 2010 *Can. Metall. Q.* **49** (3) 275
[12] Gudge K A and Jackson K A 2001 *J. Cryst. Growth* **225** 264
[13] Dragnevski K I, Cochrane R F and Mullis A M 2004 *Metall. Mater. Trans. A*. **35** 3211
[14] Battersby S E, Cochrane R F and Mullis A M 1999 *J. Mater. Sci.* **34** 2049
[15] Pohla C and Ryder P L 1997 *Acta Mater.* **45** 2155

[16] Shuleshova O, Holland-Moritz D, Loser W, Reinhart G, Iles G N and Buchner B 2009 *Europhysics Letters (EPL)*, **86**(3) 19
[17] Ilbagi A, Henein H and Phillion A B 2010 *J. Mater. Sci.*, **46** 6235
[18] Ilbagi A, Delshad Khatibi P, Swainson I P, Reinhart G and Henein H 2011 *Can. Metall. Q.,* **50**(3) 295
[19] Taylor A and Doyle N J 1972 *J. Appl. Crystallogr.* **5** 201
[20] Reutzel S, Hartmann H, Galenko P K, Schneider S and Herlach D M 2007 *Appl. Phys. Lett.* **91** 041913
[21] Piller J, Knauf R, Preu P, Herlach D M, Loho G 1986 in: *Proc. 6th Eur. Symp. on Materials Sciences under Microgravity*, (ESA SP-256, Bordeaux) p 437
[22] Herlach D M, Galenko P K 2007 *Mater. Sci. Eng. A* **449–451** 34
[23] Hyers R W, Matson D M, Kelton K F, Rogers J 2004 *Ann. NY Acad. Sci.* **1027** 474
[24] Tourret D, Gandin Ch-A 2009 *Acta Mater.* **57** 2066
[25] Tourret D, Reinhart G, Gandin Ch-A, Iles G N, Dahlborg U, Calvo-Dahlborg M, Bao C M 2011 submitted.
[26] Kurz W, Giovanola B, Trivedi R 1986 *Acta Metall. Mater.* **34** 823
[27] Jackson K A, Hunt J D 1966 *T. Metall. Soc. AIME* **236** 1129
[28] Wiskel J B, Henein H, Maire E 2002 *Can. Metall. Q.* **41** 97
[29] Hillert M 1998 *Phase Equilibrium, Phase Diagrams and Phase Transformations* (New York: Cambridge University Press)
[30] Saunders N, Miodownik A P 1998 *CALPHAD Calculation of Phase Diagrams: A Comprehensive Guide* (New York: Pergamon)
[31] Marasli N, Hunt J D 1996 *Acta Mater*. **44** 1085
[32] Smithells C J 1983 *Smithells metals reference book* (5th ed. London: Butterworths)